

Which Contrast Does Matter? Towards a Deep Understanding of MR Contrast using Collaborative GAN

Dongwook Lee¹, Won-Jin Moon² & Jong Chul Ye^{*,1}

¹*Department of Bio and Brain Engineering, KAIST, Daejeon, Korea*

²*Konkuk University Medical Center, Seoul, Korea*

Correspondence should be addressed to J.C. Y. (jong.ye@kaist.ac.kr)

Thanks to the recent success of generative adversarial network (GAN) for image synthesis, there are many exciting GAN approaches that successfully synthesize MR image contrast from other images with different contrasts. These approaches are potentially important for image imputation problems, where complete set of data is often difficult to obtain and image synthesis is one of the key solutions for handling the missing data problem. Unfortunately, the lack of the scalability of the existing GAN-based image translation approaches poses a fundamental challenge to understand the nature of the MR contrast imputation problem: which contrast does matter? Here, we present a systematic approach using Collaborative Generative Adversarial Networks (CollaGAN), which enable the learning of the joint image manifold of multiple MR contrasts to investigate which contrasts are essential. Our experimental results showed that the exogenous contrast from contrast agents is not replaceable, but other endogenous contrast such as T1, T2, etc can be synthesized from other contrast. These findings may give important guidance to the acquisition protocol design for MR in real clinical environment.

In many image processing and computer vision problems in medical imaging, a set of multiple images are usually required to find a desired output. For example, for accurate diagnosis and segmentation of the cancer margin and radiomic evaluations, multiple MR contrast such as T1-weighted (T1), post-contrast T1-weighted (T1Gd), T2 weighted (T2), and T2-FLAIR (T2F) are necessary ¹⁻³. Unfortunately, the complete set of input data are often difficult to obtain due to the different acquisition protocol at each institute, prolonged acquisition time, operator errors, or patient movement during the data acquisitions. Moreover, it is often impossible to use contrast agents for some patients with kidney failure or allergic responses. Without the complete contrast, the subsequent analysis can be prone to substantial biases and errors that can reduce the statistical efficiency of subsequent analysis ⁴, and the accurate segmentation of the whole tumor, tumor core and effective tumor core may not be feasible.

Moreover, in some situations, although multiple contrast images are available, some of the images suffers from systematic errors. For example, a synthetic MRI technique called Magnetic Resonance Image Compilation (MAGiC, GE Healthcare) ⁵ enables the generation of the various contrasts MR images using a Multi-Dynamic Multi-Echo (MDME) scan. While MAGiC can provide clinically useful synthetic MR images with various contrasts such as T1-weighted, T2-weighted, T2-FLAIR, etc, it is often reported that some of the synthetic contrasts have readily recognizable artifacts ⁵⁻⁷. Especially, the characteristic granulated hyperintense artifacts apparent in the margins along the cerebrospinal fluid (CSF)-tissue boundaries on MAGiC FLAIR can be mistaken for true pathologic conditions such as meningeal disease or subarachnoid hemorrhage in

clinical practice. Furthermore, flow and/or noise artifacts are more frequent on MAGiC FLAIR than conventional FLAIR. This often leads to the additional MR acquisition to confirm the diagnosis, which requires significant amount of cost and patient inconvenience.

Therefore, rather than re-acquiring all data as a complete set in this unexpected situation, it is often necessary to fill the missing data with substituted data. In statistical literatures, this process is often referred to as *missing data imputation*. Once all missing data have been imputed, the dataset can be used as an input for standard techniques designed for the complete dataset.

Recently, the field of image imputation has been significantly advanced thanks to the enormous success of deep neural networks⁸⁻¹². Typically, the missing image imputation problem can be formulated as an image translation problem from one domain to the other domain^{13,14}, whose performance has been greatly improved with the advance of Generative Adversarial Network (GAN)¹⁵. The main purpose of GAN architecture is to generate the realistic samples/images. Typical GAN consists of two neural networks: a generator and a discriminator. The discriminator attempts to find the features to distinguish fake image from real images, while the generator learns to synthesize images so that the discriminator is difficult to judge as real or fake. After training both neural networks, the generator produces the realistic outputs which cannot be distinguished as fake samples by the discriminator. Since the introduction of the original GAN¹⁵, many ingenious extensions have appeared. For example, for the translation between two domains A and B , CycleGAN¹³ constructs two generators, $G_{A \rightarrow B}$ and $G_{B \rightarrow A}$, and two discriminators, D_A and

D_B , so that the images between two domains can be successfully translated by cycle consistency loss ¹⁶. In another variation, to handle the multiple domains more than two, Choi et al. proposed StarGAN ¹⁴ which utilized the shared feature learning using a single generator and a single discriminator. Using the concatenated input image with target domain vector, the generator produces the fake image, which is classified as the target domain by the discriminator.

Inspired by the success of GAN-based image-translation techniques, there have been many attempt to generate MR contrast. For example, Dar et al. proposed MR contrast synthesis with conditional GAN and additional perceptual loss ¹⁷. Specifically, they utilized Pix2pix ¹⁸ and CycleGAN to translate the MR contrast images between T1 and T2 weighted images. Welander et al. compare the performance of CycleGAN and UNIT ¹⁹ in the task of translation between T1 and T2 weighted images ²⁰. Furthermore, there are severaly studies to translate the images between MR and CT (Computed Tomography) by using similar cycle consistency loss ^{16,21,22}. Meanwhile, Hagiwara et al. proposed the conditional GAN-based frameworks to generate desired FLAIR images by two step approach ²³. First, FLAIR images are generated by MAGiC. Since the MAGiC FLAIR have synthetic artifacts, they tried to remove the synthetic artifact and improve the quality of synthetic MR imaging by utilizing Pix2pix after the MAGiC.

Despite of this success, handling the multiple inputs is one of the challenges for existing image-to-image translation approaches. For example, for translating among N number of domains using CycleGAN, it is necessary to train $N(N-1)$ generators for each pair of domains, and N

discriminators for each domain. Therefore, CycleGAN requires a large number of neural networks in multi-domain setting since it is trained without feature sharing among the multi-domains. Although StarGAN¹⁴ address the multiple domain mapping, it cannot exploit the redundancies across MR contrast images to reconstruct the output contrast, since StarGAN is designed to utilize only one input.

In fact, this lack of the scalability of the existing GAN-based image translation approaches poses a fundamental challenge to understand the nature of the MR contrast imputation problem: i.e. which contrast does matter? In the age of artificial intelligence (AI) with amazing success of generative models, clinicians are interested in understanding which MR contrast is really indispensable and cannot be synthesized using a generative model. This is especially important for clinical decision making, since there are many claims that they can successfully synthesize any MR contrast. It is generally believed that the success of MR contrast is due to the redundancies in the different MR contrast. Therefore, to understand the nature of MR contrast imputation, we should understand the redundancies across many different MR contrasts to figure out what kinds of information can be, or cannot be generated. However, such an analysis is not trivial, since the understanding of the redundancies across multiple MR contrasts requires complete knowledge of joint image manifolds, which is considered as complicated machine learning task.

To address general image imputation problems in computer vision and image processing, we recently developed a novel image imputation method called Collaborative Generative Adversarial

Network (CollaGAN) ²⁴, which reconstruct the missing image by learning the redundancies across many image pairs. In CollaGAN, a set of images from the whole domains is treated as a complete set, and the network is trained to estimate the missing image by synergistically combining the information from the multiple inputs. The power of the method has been successfully demonstrated to generate facial expressions, lightning conditions, etc ²⁴.

Inspired by this success, Fig 1 illustrates how CollaGAN can be used for the case of MR contrast imputation problems. In particular, the collaborative processing of the multiple domain input images is very important in MR contrast imputation problems, since it is impossible to find the accurate pixel-intensity without understanding image manifold across different contrast. This may appear similar to MAGiC that calculates the voxel intensity from multi-contrast MR images from a MDME scan. However, in contrast to MAGiC, the collaborative learning with CollaGAN also utilizes the semantic information beyond the pixel wise relationship, so the more systematic studies about the MR contrast can be performed. Moreover, unlike CycleGAN, CollaGAN utilizes a single discriminator and a single generator to reconstruct the image of whole domains so that the generator can effectively exploit the multiple domain redundancy by learning high dimensional manifold structure across images. Specifically, by estimating specific contrast from the rest, we can understand the joint manifold structure across multiple contrast to decide which contrast is most essential and cannot be generated effectively. This is very important in clinical environment, since one can reduce the unnecessary exams while retaining the most essential one.

To validate the use of CollaGAN in understanding the essential MR contrast, we first perform quantitative study by comparing the segmentation performance by replacing one real contrast with a synthesized contrast. Here, we utilized the multi-modal brain tumor image segmentation benchmark (BraTS, 2015)^{2,3}. All the scans from BraTS consist of T1-weighted (T1), post-contrast T1-weighted (T1Gd), T2 weighted (T2), T2-FLAIR (T2F) and the ground truth segmentation labels for brain tumors. The segmentation performances were evaluated from the five different BraTS datasets: *Original*, $T1_{Colla}$, $T1Gd_{Colla}$, $T2_{Colla}$, and $T2F_{Colla}$. The datasets with subscript *Colla* represent the datasets with the substitution of a specific contrast by the reconstructed contrast from CollaGAN. Here, for brain tumor segmentation, we used the state-of-the-art segmentation network known as convolutional neural network with variational auto-encoder regularization²⁵ with some minor modifications.

Fig. 2 shows the segmentation results for the five different BraTS datasets. As shown in Fig. 2, the segmentation network performs well to find the whole tumor (WT), the tumor core (TC), and the enhancing tumor core (EC) maps on the original BraTS dataset. The segmentation maps from the synthetic BraTS datasets ($T1_{Colla}$, $T2_{Colla}$, $T2F_{Colla}$ and $T1Gd_{Colla}$) produced similar results to the ground truth and the result maps from the original BraTS. For quantitative evaluation, we measured the segmentation performance by the dice similarity score²⁶ between the prediction map, Y_{pred} , and the ground truth, Y_{gt} :

$$Dice(Y_{gt}, Y_{pred}) = \frac{2|Y_{gt} \cap Y_{pred}|}{|Y_{gt}| + |Y_{pred}|},$$

where $|\cdot|$ represents the cardinalities of the set (number of elements in each set). The segmen-

tation network achieves $0.8531 \pm 0.0869 / 0.7368 \pm 0.1850 / 0.7066 \pm 0.2717$ (mean \pm std, $N=28$) DICE scores for WT / TC / EC, respectively, when using the original BraTS datasets. When the original T1-weighted images are replaced with the reconstructed image by CollaGAN ($T1_{Colla}$), the DICE scores are reaches to $0.8567 \pm 0.0882 / 0.7342 \pm 0.1857 / 0.6979 \pm 0.2718$ for WT / TC / EC, respectively, without any additional training or fine-tuning process. The segmentation performance between the original and ($T1_{Colla}$, $T2_{Colla}$, and $T2F_{Colla}$) are very similar as shown in Fig. 5. The results validated the reconstructed contrast images by CollaGAN for the data set $T1_{Colla}$, $T2_{Colla}$, and $T2F_{Colla}$ are very similar to the original contrast images from the original BraTS dataset.

However, the injection of the gadolinium contrast agent provides additional tissue information so that the post-contrast T1-weighted (T1Gd) images show important role in the segmentation of TC and EC as shown in the performance drop of the segmentation results using $T1Gd_{Colla}$. While the performance drop from CollaGAN reconstructed T1Gd images using the other contrasts is relatively small for WT and TC in Fig. 3, the performance drop in EC is statistically significant. This experimental provides systematic understanding that the information of contrast injection is still indispensable unless additional diagnostic evaluation is performed. This is as expected given the wide use of MR contrast agent.

Although the previous experiment shows that the gadolinium contrast cannot be synthesized accurately, it also shows promising results that intrinsic MR contrast may be estimated from the

remaining intrinsic contrasts. Thus, we investigate whether collaborative learning can essentially overcome the limitation of MAGiC images. As shown in Fig. 4 (a-b), accurate contrast was generated using CollaGAN by synergistically utilizing the redundancies across the remaining contrast. In contrast to CycleGAN and StarGAN that utilize a single input MR image, the accurate reconstructions of the voxel intensity are only possible by synergistically combining multiple contrast information via CollaGAN. To verify the clinical efficacy of the method, the reconstructed MR contrast images were undergone radiological evaluation. The CollaGAN performs very well not only for the brain MR images from the normal subjects, but also for the brain scans from the subjects with lesions (Fig. 5 (a-b)). The hyperintensity signal of the CSF space (yellow circled in Fig. 5(a)) compared to the other side hemisphere is well reconstructed on both MAGiC T2-FLAIR and T2-FLAIR. Here, MAGiC T2-FLAIR and T2-FLAIR refer to the synthetic T2-FLAIR by MAGiC and the true T2-FLAIR contrast by additional acquisition, respectively. The cortical and sulcal abnormality (yellow circled in Fig. 5 (b)) are also visible on the reconstructed MAGiC T2-FLAIR and T2-FLAIR. The lesions of the subjects are well reconstructed compared to the original scans. On the other hand, even if there exists systemic artifact on synthetic MAGiC T2-FLAIR, CollaGAN still reconstructs the artifact-free T2-FLAIR results with a help from the collaborative input as shown in Fig. 5 (c-d). The focal sulcal hyperintensity (yellow arrow in Fig. 5 (c)) is only visible on T2-FLAIR (both original and reconstructed) while it is not visible on MAGiC T2-FLAIR images. Since the synthetic images (T1-FLAIR, T2-weighted, MAGiC T2-FLAIR) from MAGiC cannot capture the aforementioned hyper-intensity, it is usual to acquire additional scan of T2-FLAIR to detect the lesion. However, the hyper-intensity lesion could be detected on the reconstructed T2-

FLAIR by CollaGAN. Also, in the reconstructed MAGiC T2-FLAIR, there exists a pseudo-lesion (yellow arrow in Fig. 5(d)) which is not visible on both original and reconstructed T2-FLAIR. The radiologist concludes that the reconstructed conventional T2-FLAIR contrast from CollaGAN not only reflects the original contrast well, but also removes the systemic artifacts from MAGiC well. By reconstructing the specific desired contrast MR images without any artifacts, we could save the scan time by avoiding the additional scan for accurate clinical diagnosis.

In conclusion, we employ a novel architecture, CollaGAN, to investigate the essential MR contrast for imaging study, since CollaGAN can impute missing image by synergistically learning the joint image manifold of multiple MR contrasts. Using the segmentation study, we found that images from the contrast agent are indispensable and cannot be completely replaced by generative models. For the case of intrinsic contrasts such as T2-FLAIR, we demonstrated that CollaGAN reconstructs the specific contrast MR images without any artifacts, so that it can the scan time by avoiding the additional scan for accurate clinical diagnosis. Our proposed CollaGAN model can be utilized for all other types of imaging studies to investigate which contrast is the most essential and which contrast is redundant.

METHODS

Background Theory for CollaGAN Here, we explain our Collaborative GAN framework to handle multiple inputs for generating more realistic output for image imputation. For ease of explanation, we assume that there are four types ($N = 4$) of domains: a , b , c , and d . To handle the

multiple-inputs using a single generator, we train the generator to synthesize the output image in the target domain, \hat{x}_a , using a collaborative mapping from the set of the other types of multiple images, $\{x_a\}^C = \{x_b, x_c, x_d\}$, where the superscript C denotes the complementary set. This mapping is formally described by

$$\hat{x}_\kappa = G(\{x_\kappa\}^C; \kappa) \quad (1)$$

where $\kappa \in \{a, b, c, d\}$ denotes the target domain index that guides to generate the output of the proper target domain, κ . As there are N number of combinations for single-output and its corresponding complementary set as multiple-inputs, we randomly choose these combination during the training so that the generator learns the various mappings to the multiple target domains.

One of the key concepts for the proposed method is the *multiple cycle consistency*. Since the original cycle-consistency loss cannot be defined for the multiple inputs, the cyclic loss should be redefined. Suppose that the *fake* output from the forward cycle for the generator, G , is \hat{x}_a . Then, we could generate $N - 1$ number of new inputs by the combinations with the *fake* output, \hat{x}_a , and the inputs, x_b, x_c, x_d . Using the new combination inputs, the generator synthesizes the *reconstructed* outputs, $\tilde{x}_{\cdot|a}$, for the backward flow of the cycle. For example, when $N = 4$, there are three combinations of multi-input and single-output so that we can reconstruct the three images

of original domains using backward flow of the generator as:

$$\tilde{x}_{b|a} = G(\{\hat{x}_a, x_c, x_d\}; b)$$

$$\tilde{x}_{c|a} = G(\{\hat{x}_a, x_b, x_d\}; c)$$

$$\tilde{x}_{d|a} = G(\{\hat{x}_a, x_b, x_c\}; d)$$

Then, the associated multiple cycle consistency loss can be defined as following:

$$\mathcal{L}_{mcc,a} = \|x_b - \tilde{x}_{b|a}\|_1 + \|x_c - \tilde{x}_{c|a}\|_1 + \|x_d - \tilde{x}_{d|a}\|_1$$

where $\|\cdot\|_1$ is the l_1 -norm. In general, the multiple cycle consistency loss for the multiple domains κ can be written by

$$\mathcal{L}_{mcc,\kappa} = \sum_{\kappa' \neq \kappa} \|x_{\kappa'} - \tilde{x}_{\kappa'|\kappa}\|_1 \quad (2)$$

where

$$\tilde{x}_{\kappa'|\kappa} = G(\{\hat{x}_\kappa\}^C; \kappa') \quad (3)$$

To use a single generator, we need to use the mask vector to guide the generator to the target domain. The mask vector is an one-hot encoding vector which represents the target domain. When it is fed into the encoder part of G (Fig. 6 left), it is enlarged as same dimension with the input images to be easily concatenated. The mask vector has N class number of channel dimension to represent the target domain as one-hot encoding along the channel dimension. This is a simplified version of mask vector which was originally introduced in StarGAN¹⁴.

Discriminator Loss As mentioned before, the discriminator has two roles: one is to classify the source which is real or fake, and the other is to classify the type of domain which is class a, b, c or d . Therefore, the discriminator loss consists of two parts: adversarial loss and domain classification loss. This can be realized using the two sub-paths D_{gan} and D_{clsf} in a single discriminator that shares the same neural network weights for feature extraction except the last layers for sub-paths.

Specifically, the adversarial loss is necessary to make the generated images as realistic as possible. The regular GAN loss may lead to the vanishing gradients problem during the learning process^{27,28}. To overcome such problem and improve the robustness of the training, the adversarial loss of Least Square GAN²⁷ was utilized instead of the original GAN loss. In particular for the optimization of the discriminator, D_{gan} , the following loss is minimized:

$$\mathcal{L}_{gan}^{disc}(D_{gan}) = \mathbb{E}_{x_{\kappa}}[(D_{gan}(x_{\kappa}) - 1)^2] + \mathbb{E}_{\tilde{x}_{\kappa|\kappa}}[(D_{gan}(\tilde{x}_{\kappa|\kappa}))^2],$$

whereas the generator is optimized by minimizing the following loss:

$$\mathcal{L}_{gan}^{gen}(G) = \mathbb{E}_{\tilde{x}_{\kappa|\kappa}}[(D_{gan}(\tilde{x}_{\kappa|\kappa}) - 1)^2]$$

where $\tilde{x}_{\kappa|\kappa}$ is defined in (3).

Next, the domain classification loss consists of two parts: $\mathcal{L}_{clsf}^{real}$ and $\mathcal{L}_{clsf}^{fake}$. They are the cross entropy loss for domain classification from the real images and the fake image, respectively. Recall that the goal of training G is to generate the image properly classified to the target domain. Thus, we first need a best classifier D_{clsf} that should be trained only with the real data to guide the

generator properly. Accordingly, we first minimize the loss $\mathcal{L}_{clsf}^{real}$ to train the classifier D_{clsf} , then $\mathcal{L}_{clsf}^{fake}$ is minimized by training G with fixing D_{clsf} so that the generator can be trained to generate samples that can be classified correctly.

Specifically, to optimize the D_{clsf} , the following $\mathcal{L}_{clsf}^{real}$ should be minimized with respect to D_{clsf} :

$$\mathcal{L}_{clsf}^{real}(D_{clsf}) = \mathbb{E}_{x_\kappa} [-\log(D_{clsf}(\kappa; x_\kappa))] \quad (4)$$

where $D_{clsf}(\kappa; x_\kappa)$ can be interpreted as the probability to correctly classify the real input x_κ as the class κ . On the other hand, the generator G should be trained to generate fake samples which are properly classified by the D_{clsf} . Thus, the following loss should be minimized with respect to G :

$$\mathcal{L}_{clsf}^{fake}(G) = \mathbb{E}_{\hat{x}_{\kappa|\kappa}} [-\log(D_{clsf}(\kappa; \hat{x}_{\kappa|\kappa}))] \quad (5)$$

Structural Similarity Index Loss Structural Similarity (SSIM) index is one of the state-of-the-art metrics to measure the image quality²⁹. The l_2 loss, which is widely used for the image restoration tasks, has been reported to cause the blurring artifacts on the results^{30–32}. SSIM is one of the perceptual metrics and it is also differentiable, so it can be backpropagated³². The SSIM for pixel p is defined as

$$\text{SSIM}(p) = \frac{2\mu_X\mu_Y + C_1}{\mu_X^2 + \mu_Y^2 + C_1} \cdot \frac{2\sigma_{XY} + C_2}{\sigma_X^2 + \sigma_Y^2 + C_2} \quad (6)$$

where μ_X is an average of X , σ_X^2 is a variance of X and σ_{XX^*} is a covariance of X and X^* . There

are two variables to stabilize the division such as $C_1 = (k_1 L)^2$ and $C_2 = (k_2 L)^2$. L is a dynamic range of the pixel intensities. k_1 and k_2 are constants by default $k_1 = 0.01$ and $k_2 = 0.03$. Since the SSIM is defined between 0 and 1, the loss function for SSIM can be written by:

$$\mathcal{L}_{\text{SSIM}}(X, Y) = -\log \left(\frac{1}{2|P|} \sum_{p \in P(X, Y)} (1 + \text{SSIM}(p)) \right) \quad (7)$$

where P denotes the pixel location set and $|P|$ is its cardinality. The SSIM loss was applied as an additional multiple cycle consistency loss as follows:

$$\mathcal{L}_{\text{mcc-SSIM}, \kappa} = \sum_{\kappa' \neq \kappa} \mathcal{L}_{\text{SSIM}}(x_{\kappa'}, \tilde{x}_{\kappa'|\kappa}). \quad (8)$$

Generator CollaGAN consists of single pair of a generator, G , and a discriminator, D . For the generator, we redesigned U-net³³ structure with the following three modification: CCNL (series of convolutions, concatenation, normalization, and Leaky-ReLU layer) unit, multi-branched encoder, and channel attention as shown in Fig. 6.

First, the modified U-net basically consists of CCNL unit instead of CBR unit (series of convolution, batch normalization and ReLU layer) in original U-net architecture. Similar to the multi-resolution approach of GoogLeNet³⁴, CCNL unit has two branched inputs: 1×1 convolution and 3×3 convolution layer. The two convolution layers are concatenated and pass through the Leaky-ReLU layer as shown in Fig. 6. It is important to utilize the 1×1 convolution since the voxel-wise synthesis of the reconstruction is necessary as well as the 3×3 convolution feature extraction for large receptive field. Thus, two branches of feature information are parallelly processed in CCNL units.

Second, we designed a multi-branched encoder for individual feature extraction for each input images (Fig. 6 left). The generator consists of two parts: encoder and decoder. In the encoding step, each image are encoded separately by four branches. Here, the mask vector is concatenated to every input images to extract the proper features for the target domain. Then, the encoded features are concatenated at the end of the encoder and the concatenated features are fed into the decoder with the contracting paths between encoder and decoder. Since the inputs are not simply mixed in the first layer, the separated features for each contrast image are extracted with a help of the multi-branched encoder.

Third, the channel attention module called CCAM (Conditional Channel Attention Module) ³⁵ is applied to the decoder part of the generator with the following modifications. CCAM was originally designed for image translation to mixed-domain using Sym-parameterized Generative Network (SGN) ³⁵. CCAM selectively excludes channels and reduces influences of unnecessary channels to generate images in a mixed-domain conditioned by sym-parameters. Here, we applied channel attention in the decoder part of the generator by CCAM modules using the one-dimensional mask vector as a sym-parameter. The input mask and the average pooled input features are concatenated and pass through the attention-MLP (multi-layered perceptron). The channel attentions are calculated as a form of scaling weights for each channel of input feature:

$$CCAM(X, m) = X \cdot \sigma(MLP([P_{avg}(X), m]))$$

where X and m represent the input features and 1-D input mask vector for target domain, respectively. And P_{avg} , σ and \cdot are the average pooling, the sigmoid operation and the elementwise

multiplication, respectively. The refined features are calculated by the element-wise multiplication between input features, X , and the scaling weights. The CCAM module chooses the channels with the calculated attention according to the target domain and the input features.

Discriminator To classify the contrast of the MR images, the feature extraction by the multi-resolution processing is important. This kind of multi-scale approach is reported to work well in the classification of MR contrasts³⁶. The discriminator has three branches that have different scales of resolution. Specifically, the first branch extracts the feature at the original scale of resolution and then reduces the size of feature domain. Another branch processes the feature extraction on the quarter resolution scales ($height/4$, $width/4$). The other branch sequentially reduces the scales by two for extracting features. These three branches are concatenated to gather the features in multi-scale manner. After that, the discriminator consists of three series of convolution with stride two and Leaky-ReLU. At the end of the discriminator, there are two output headers: one is the source classification header for real or fake and the other is the domain classification header. PatchGAN^{13,18} was utilized on the source classification header to classify whether local image patches are real or fake. We also found that the dropout^{37,38} was very effective to prevent the overfitting of the discriminator.

Brain Tumor segmentation datasets For quantitative analysis for the reconstruction performance, the multimodal brain tumor image segmentation benchmark (BraTS, 2015)^{2,3} was used. BraTS supplies the routine clinically-acquired 3T multimodal MRI scans and the ground truth labels for

brain tumor segmentation. The ground truth labels have been manually-revised by the expert board-certified neuroradiologists. The routine MRI scans consist of four different contrasts including native (T1), post-contrast T1-weighted (T1Gd), T2-weighted (T2), and T2-FLAIR (T2F) volumes, and were acquired with different clinical protocols and various scanners from multiple institutions. The datasets were divided into 218 / 28 / 28 subjects for train / validation / test sets, respectively.

Tumor segmentation algorithm A semantic segmentation network for brain tumor segmentation from 3D MRIs using autoencoder regularization²⁵ achieved the top performance score in BraTS 2018 challenge. We implemented the segmentation network with some modifications to handle memory efficiently.

The segmentation network consists of shared encoder part and two branches of decoder part. The encoder has an asymmetrically larger CNN architecture compared to the decoder part, to extract the features from the inputs. To fit into GPU memory size, we modified the 3D convolution layer to 2D convolution layer to perform 2.5D segmentation instead of 3D, which utilize the multiple neighborhood slices of MR images to map the single segmentation label. Here, we choose five slices (two adjacent slices from each dorsal and ventral slice) as input to find the tumor segmentation maps of the center slice. The encoder part uses the blocks where each block consists of two convolutions with Group normalization (GN)³⁹ and ReLU, followed by additive identity skip connection. After the two unit blocks in each spatial level, the image dimensions were progres-

sively downsized by two using the strided convolutions, and simultaneously increased feature size by two.

One branch of the decoder is for the segmentation map. The decoder reconstructs each of the segmentation maps for following three tumor subregions: whole tumor, tumor core, and enhancing tumor core. The decoder utilised the same blocks in the encoder, but with a single block per each spatial level. The other branch of the decoder is for the regularization. The additional variational auto-encoder (VAE) branch reconstructs the input image itself to regularize the shared encoder during the training phase. The VAE branch was added to the encoder endpoint which is similar to auto-encoder architecture to additional guidance and regularization to the encoder part.

Synthetic MR datasets We prepared the four types of contrasts for 280 axial brain images from 10 subjects. The subjects were scanned by the multi-dynamic multi-echo (MDME) sequence and the additional T2-FLAIR (FLuid-Attenuated Inversion Recovery) sequences. Synthetic T1-FLAIR (T1F), T2-weighted (T2w) and MAGiC T2-FLAIR (T2F) images were acquired from MAGnetic resonance image Compilation (MAGiC, GE Healthcare) ⁵ using the MDME scans. The MR scan parameters for T1-FLAIR / T2-weighted / MAGiC T2-FLAIR are as followings: TR 2500ms, TE 10ms, TI 1050ms, FA 90° / TR 3500ms, TE 128ms, FA 90° / TR 9000ms, TE 95ms, TI 2408ms, FA 90°, respectively. The additional T2-FLAIR scans was acquired with different scan parameter of T2F: TR 9000ms, TE 93ms, TI 2471ms, FA 160°. The followings are common parameters for four scans: FOV 220×220mm, 320×224 acquisition matrix, 4.0mm slice thickness. The MR

images were divided into the train (224 images), validation (28 images) and test sets (28 images) by the subjects.

Data preprocessing and Augmentation The MR images were normalized to have unit standard deviations based on the non-zero-voxels only. For the data augmentation, we apply a random scale (0.9-1.1) and a random flip on lateral-to-lateral direction with a probability 0.5.

1. Drevelegas, A. & Papanikolaou, N. Imaging modalities in brain tumors. In *Imaging of Brain Tumors with Histological Correlations*, 13–33 (Springer, 2011).
2. Menze, B. H. *et al.* The multimodal brain tumor image segmentation benchmark (brats). *IEEE transactions on medical imaging* **34**, 1993–2024 (2015).
3. Bakas, S. *et al.* Advancing the cancer genome atlas glioma mri collections with expert segmentation labels and radiomic features. *Scientific data* **4**, 170117 (2017).
4. Baraldi, A. N. & Enders, C. K. An introduction to modern missing data analyses. *Journal of school psychology* **48**, 5–37 (2010).
5. Tanenbaum, L. N. *et al.* Synthetic MRI for clinical neuroimaging: Results of the Magnetic Resonance Image Compilation (MAGiC) prospective, multicenter, multireader trial. *American Journal of Neuroradiology* (2017).
6. Hagiwara, A. *et al.* Synthetic mri in the detection of multiple sclerosis plaques. *American Journal of Neuroradiology* **38**, 257–263 (2017).
7. Hagiwara, A. *et al.* Symri of the brain: rapid quantification of relaxation rates and proton density, with synthetic mri, automatic brain segmentation, and myelin measurement. *Investigative radiology* **52**, 647 (2017).

8. Krizhevsky, A., Sutskever, I. & Hinton, G. E. Imagenet classification with deep convolutional neural networks. In *Advances in neural information processing systems*, 1097–1105 (2012).
9. Zhang, K., Zuo, W., Chen, Y., Meng, D. & Zhang, L. Beyond a gaussian denoiser: Residual learning of deep cnn for image denoising. *IEEE Transactions on Image Processing* **26**, 3142–3155 (2017).
10. Dong, C., Loy, C. C., He, K. & Tang, X. Image super-resolution using deep convolutional networks. *IEEE transactions on pattern analysis and machine intelligence* **38**, 295–307 (2016).
11. Xie, J., Xu, L. & Chen, E. Image denoising and inpainting with deep neural networks. In *Advances in neural information processing systems*, 341–349 (2012).
12. Deng, J. *et al.* Imagenet: A large-scale hierarchical image database. In *Computer Vision and Pattern Recognition, 2009. CVPR 2009. IEEE Conference on*, 248–255 (Ieee, 2009).
13. Zhu, J.-Y., Park, T., Isola, P. & Efros, A. A. Unpaired image-to-image translation using cycle-consistent adversarial networks. *arXiv preprint* (2017).
14. Choi, Y. *et al.* StarGAN: Unified generative adversarial networks for multi-domain image-to-image translation. *arXiv preprint* **1711** (2017).
15. Goodfellow, I. *et al.* Generative adversarial nets. In *Advances in neural information processing systems*, 2672–2680 (2014).

16. Wolterink, J. M. *et al.* Deep mr to ct synthesis using unpaired data. In *International Workshop on Simulation and Synthesis in Medical Imaging*, 14–23 (Springer, 2017).
17. Dar, S. U. *et al.* Image synthesis in multi-contrast mri with conditional generative adversarial networks. *IEEE transactions on medical imaging* (2019).
18. Isola, P., Zhu, J.-Y., Zhou, T. & Efros, A. A. Image-to-image translation with conditional adversarial networks. *arXiv preprint* (2017).
19. Liu, M.-Y., Breuel, T. & Kautz, J. Unsupervised image-to-image translation networks. In *Advances in Neural Information Processing Systems*, 700–708 (2017).
20. Welander, P., Karlsson, S. & Eklund, A. Generative adversarial networks for image-to-image translation on multi-contrast mr images—a comparison of cyclegan and unit. *arXiv preprint arXiv:1806.07777* (2018).
21. Yang, H. *et al.* Unpaired brain mr-to-ct synthesis using a structure-constrained cyclegan. In *Deep Learning in Medical Image Analysis and Multimodal Learning for Clinical Decision Support*, 174–182 (Springer, 2018).
22. Hiasa, Y. *et al.* Cross-modality image synthesis from unpaired data using cyclegan. In *International Workshop on Simulation and Synthesis in Medical Imaging*, 31–41 (Springer, 2018).
23. Hagiwara, A. *et al.* Improving the quality of synthetic flair images with deep learning using a conditional generative adversarial network for pixel-by-pixel image translation. *American Journal of Neuroradiology* **40**, 224–230 (2019).

24. Lee, D., Kim, J., Moon, W.-J. & Ye, J. C. CollaGAN: Collaborative GAN for missing image data imputation. *to appear in Proc. of IEEE Conf. on Computer Vision and Pattern Recognition (CVPR), also available as arXiv preprint arXiv:1901.09764* (2019).
25. Myronenko, A. 3D MRI brain tumor segmentation using autoencoder regularization. *arXiv preprint arXiv:1810.11654* (2018).
26. Dice, L. R. Measures of the amount of ecologic association between species. *Ecology* **26**, 297–302 (1945).
27. Mao, X. *et al.* Least squares generative adversarial networks. In *Computer Vision (ICCV), 2017 IEEE International Conference on*, 2813–2821 (IEEE, 2017).
28. Arjovsky, M., Chintala, S. & Bottou, L. Wasserstein GAN. *arXiv preprint arXiv:1701.07875* (2017).
29. Wang, Z., Bovik, A. C., Sheikh, H. R. & Simoncelli, E. P. Image quality assessment: from error visibility to structural similarity. *IEEE transactions on image processing* **13**, 600–612 (2004).
30. Ledig, C. *et al.* Photo-realistic single image super-resolution using a generative adversarial network. In *CVPR*, vol. 2(3), 4 (2017).
31. Mathieu, M., Couprie, C. & LeCun, Y. Deep multi-scale video prediction beyond mean square error. *arXiv preprint arXiv:1511.05440* (2015).

32. Zhao, H., Gallo, O., Frosio, I. & Kautz, J. Loss functions for image restoration with neural networks. *IEEE Transactions on Computational Imaging* **3**, 47–57 (2017).
33. Ronneberger, O., Fischer, P. & Brox, T. U-net: Convolutional networks for biomedical image segmentation. In *International Conference on Medical image computing and computer-assisted intervention*, 234–241 (Springer, 2015).
34. Szegedy, C. *et al.* Going deeper with convolutions. In *Proceedings of the IEEE conference on computer vision and pattern recognition*, 1–9 (2015).
35. Chang, S., Park, S., Yang, J. & Kwak, N. Image translation to mixed-domain using sym-parameterized generative network. *arXiv preprint arXiv:1811.12362* (2018).
36. Remedios, S., Pham, D. L., Butman, J. A. & Roy, S. Classifying magnetic resonance image modalities with convolutional neural networks. In *Proc. of SPIE Vol*, vol. 10575, 105752I–1 (2018).
37. Hinton, G. E., Srivastava, N., Krizhevsky, A., Sutskever, I. & Salakhutdinov, R. R. Improving neural networks by preventing co-adaptation of feature detectors. *arXiv preprint arXiv:1207.0580* (2012).
38. Srivastava, N., Hinton, G., Krizhevsky, A., Sutskever, I. & Salakhutdinov, R. Dropout: a simple way to prevent neural networks from overfitting. *The Journal of Machine Learning Research* **15**, 1929–1958 (2014).
39. Wu, Y. & He, K. Group normalization. *arXiv preprint arXiv:1803.08494* (2018).

Acknowledgements This research was supported by the National Research Foundation (NRF) of Korea grant NRF-2016R1A2B3008104.

Competing Interests The authors declare that they have no competing financial interests.

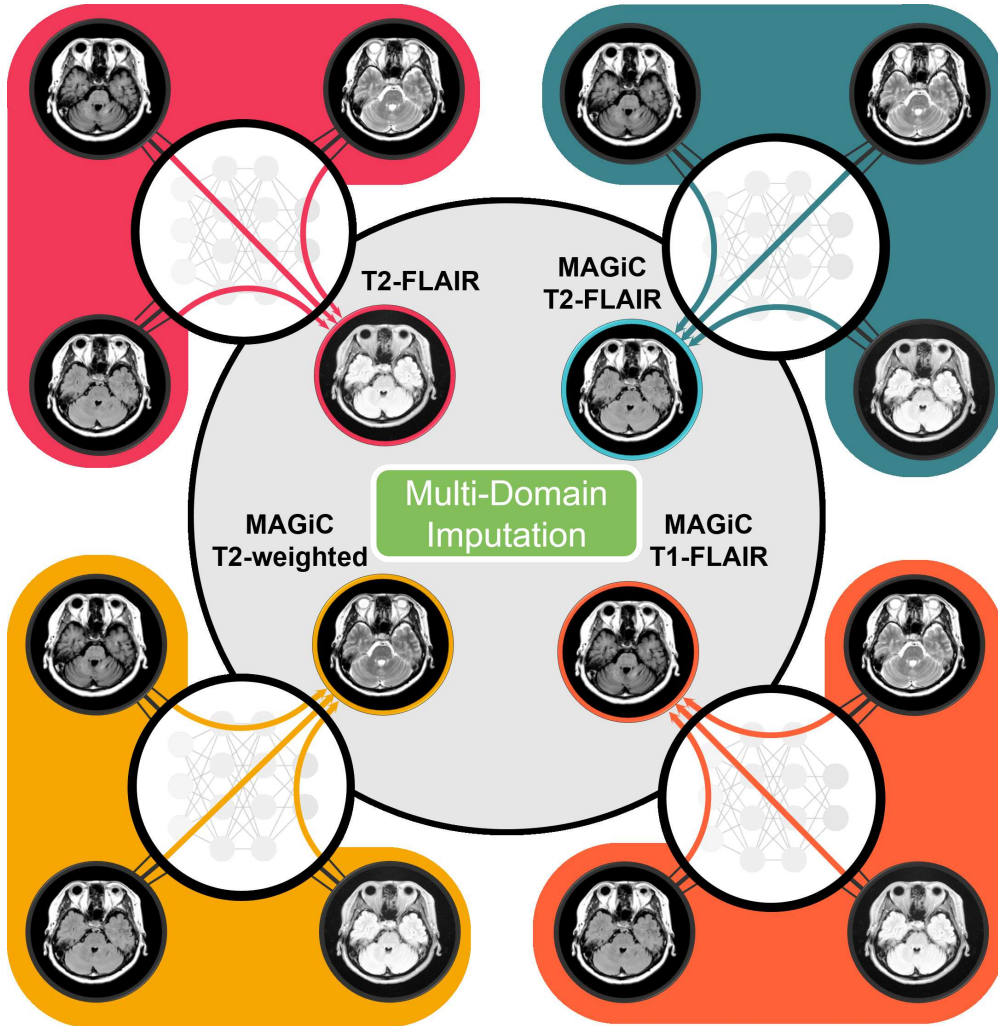


Figure 1: Concept diagram of multi-domain imputation task on MR contrast images using the proposed Collaborative GAN (CollaGAN). The single generator (black circle) of CollaGAN utilizes multiple input images from various contrasts to synthesize the target contrast image. Here, T1-FLAIR (orange circle), T2-weighted (yellow circle), MAGiC T2-FLAIR (green circle) from synthetic MR imaging (MAGiC) and the additional scan by conventional T2-FLAIR (red circle) were used for multi-domain imputation.

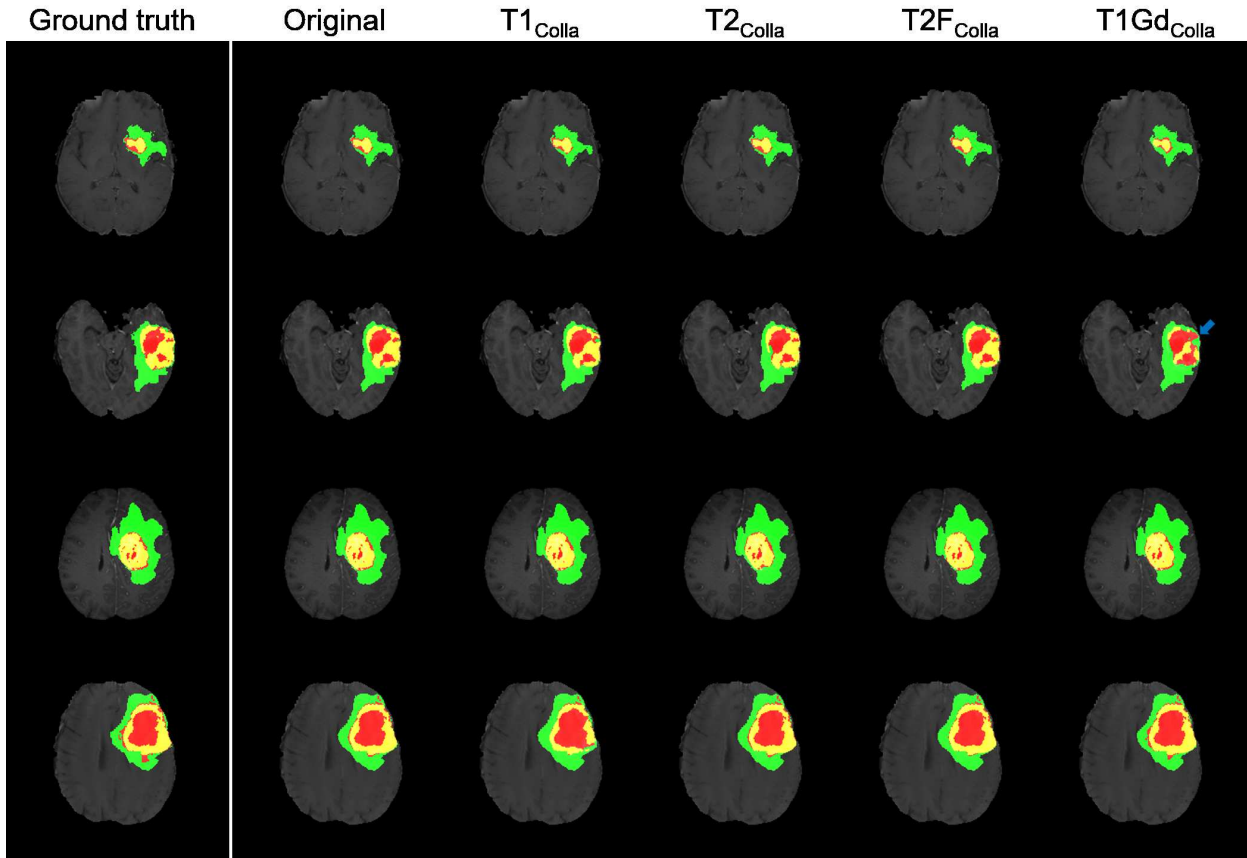


Figure 2: BRaTS segmentation results for quantitative evaluation of CollaGAN. The labels of the whole tumor (union of green, red and yellow), the tumor core (union of red and yellow), and the enhancing tumor core (yellow) are overlaid on T1-weighted sagittal images. The segmentation results from the original BRaTS datasets (2nd row) show similar to the ground truth (1st row). $T1_{Colla}$, $T2_{Colla}$, $T2F_{Colla}$, and $T1Gd_{Colla}$ represent the datasets which the T1 weighted images, T2 weighted images, T2-FLAIR, and T1 weighted images with Gd-injection are respectively substituted by the reconstructed images from CollaGAN. For whole tumor, tumor core and enhancing tumor core, it shows the similar segmentation performance on both the original BRaTS and the reconstructed BRaTS datasets from CollaGAN. In $T1Gd_{Colla}$ (last row), the prediction of enhancing tumor core shows inferior performance (blue arrows) since $T1Gd_{Colla}$ has the lack of the information from the Gd-injection which is necessary to predict accurate enhancing tumor core region.

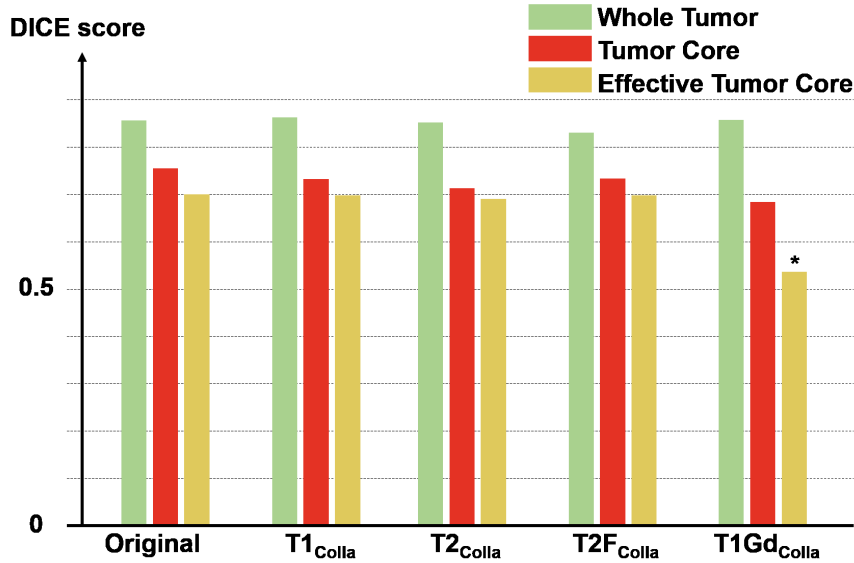


Figure 3: Quantitative results for segmentation performance using the following datasets: original BRaTS and $T1_{Colla}$, $T2_{Colla}$, $T2F_{Colla}$, and $T1Gd_{Colla}$ data set. Here, $T1_{Colla}$, $T2_{Colla}$, $T2F_{Colla}$, and $T1Gd_{Colla}$ represent the datasets which the T1 weighted images, T2 weighted images, T2-FLAIR and T1 weighted images with Gd-injection are respectively substituted by the reconstructed images from CollaGAN. The segmentation network shows similar performance for the whole tumor, the tumor core, and enhancing tumor core on both the original BRaTS and the reconstructed datasets by CollaGAN for $T1_{Colla}$, $T2_{Colla}$, and $T2F_{Colla}$ data set. However, the prediction of enhancing tumor core shows inferior performance in $T1Gd_{Colla}$, since $T1Gd_{Colla}$ is lack of the information from the Gd-injection which is necessary for accurate prediction of the enhancing tumor core region.

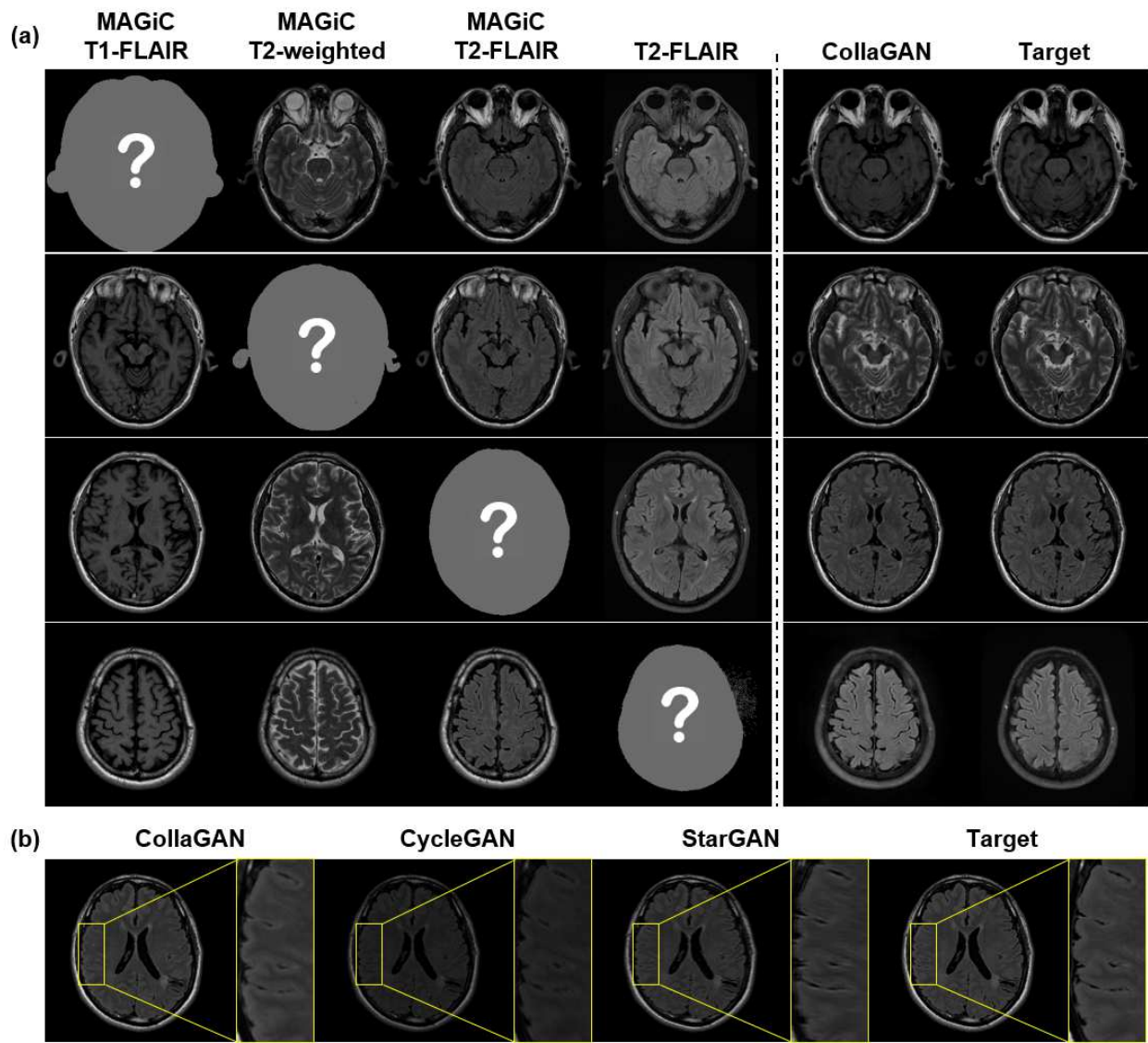


Figure 4: (a) MR contrast imputation results using the proposed method, CollaGAN. The target domain contrast images (right) were reconstructed from the other contrast inputs (left). The contrast image to impute is marked as the question mark. The normalized mean squared error (NMSE) and the structural similarity index (SSIM) of the results are as following (NMSE/SSIM): 0.0326/0.918 for T1-FLAIR, 0.109/0.904 for T2-weighted, 0.0238/0.942 for MAGiC T2-FLAIR, and 0.110/0.740 for T2-FLAIR. (b) Comparison of T2-FLAIR imputation results using CycleGAN, StarGAN and CollaGAN with $\times 3$ magnified images.

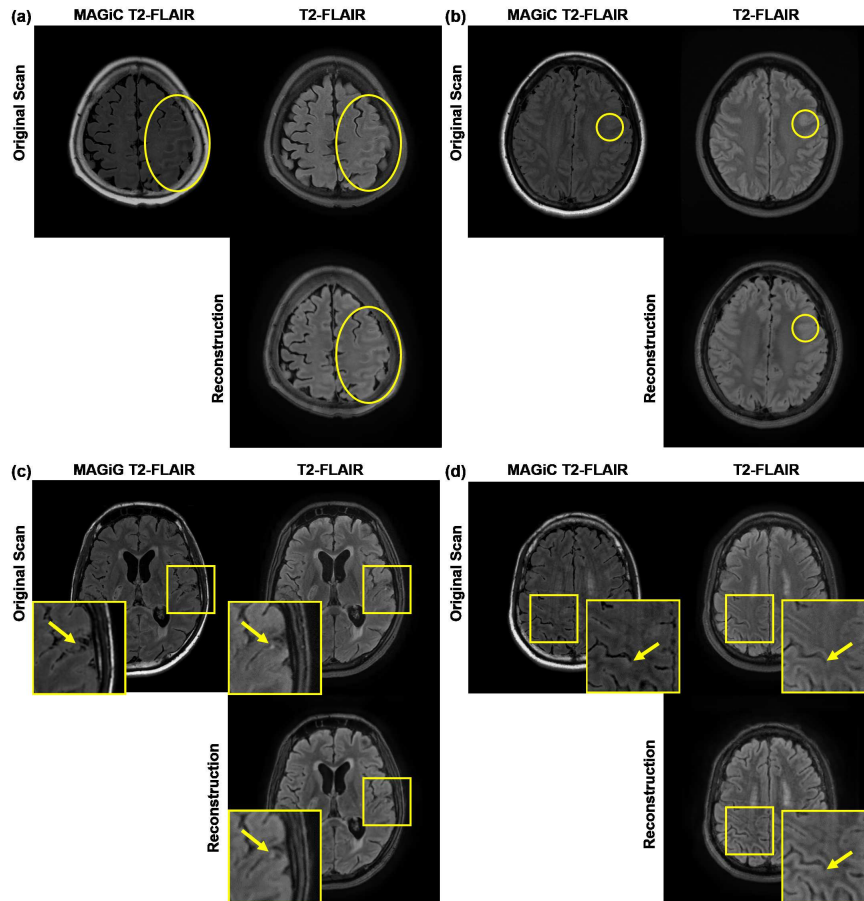


Figure 5: Reconstruction results with lesions by CollaGAN. MAGiC T2-FLAIR, the ground truth (T2-FLAIR, separated conventional scan), and the reconstructed T2-FLAIR using CollaGAN are illustrated. When there is no synthetic artifact on MAGiC T2-FLAIR (a-b), the reconstructed contrasts from CollaGAN also show the accurate performance. (a) The hyperintensity signal of the CSF space (circled) compared to the other side hemisphere is visible on all three images. (b) The cortical and sulcal abnormality (circled) is also visible on all three images. On the other hand, although there exists synthetic artifact on MAGiC T2-FLAIR (c-d), CollaGAN reconstructs the artifact-free T2-FLAIR results similar to the ground-truth T2-FLAIR images. (c) The focal sulcal hyperintensity (arrow) is only visible on original T2-FLAIR and reconstruction T2-FLAIR by CollaGAN, while it is not visible on the MAGiC T2-FLAIR images. The MAGiC T2-FLAIR cannot capture the hyperintensity lesion, but CollaGAN can accurately capture it. (d) In MAGiC T2-FLAIR, there is a pseudo-lesion (arrow) which is not visible on both original T2-FLAIR and reconstructed T2-FLAIR by CollaGAN.

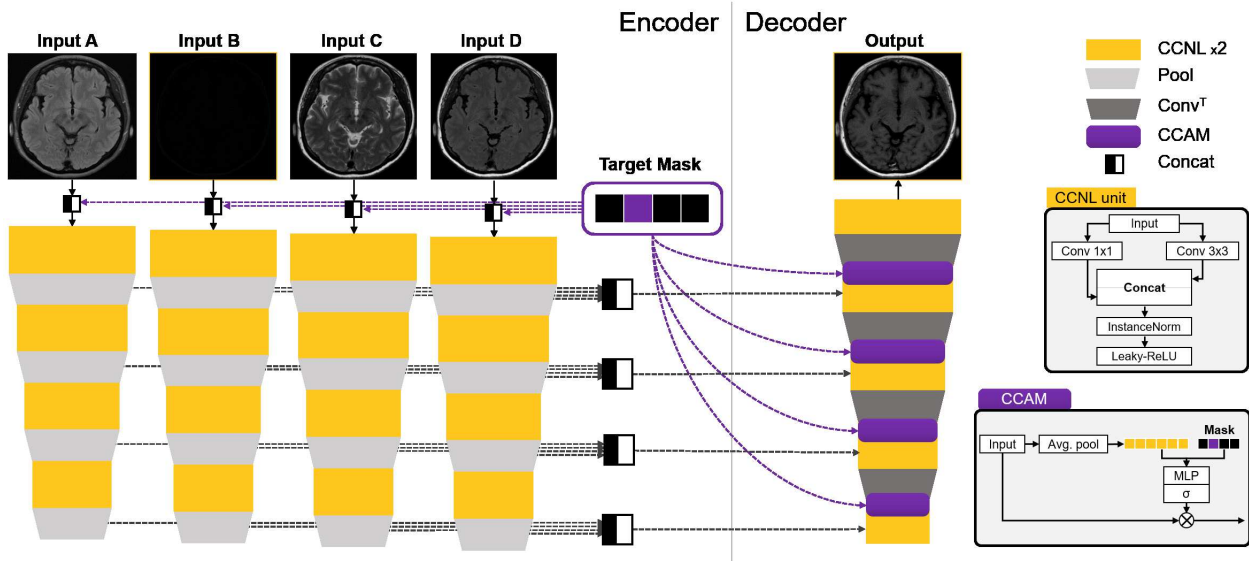


Figure 6: Architecture of the generator used for MR contrast imputation. The input images were concatenated with the target mask which represents the target domain. The network consists of CCNL unit (Concatenation of two Convolutions followed by instance Normalization and Leaky-relu, yellow), pooling layer (grey), convolution transpose layer (dark grey), concatenate layer (half black/white square), and CCAM (Conditioned Channel Attention Module, purple). The network is divided by encoder part and decoder part. The encoder is multi-branched for individual feature extraction of each input MR contrast. The decoder part consists of series of CCNL units and CCAM. The CCAM gives the attention for accurate reconstruction of the contrast image in the target domain.